Largest aftershock nucleation driven by afterslip during the 2014 Iquique sequence

Yuji Itoh[1,2,*], Anne Socquet[1], and Mathilde Radiguet[1]

[1]Univ. Grenoble Alpes, Univ. Savoie Mont Blanc, CNRS, IRD, Univ. Gustave Eiffel, ISTerre, 38000 Grenoble, France.

[2]Earthquake Research Institute, The University of Tokyo, Tokyo, Japan.

*Corresponding author: Yuji Itoh (yitoh@eri.u-tokyo.ac.jp)

Key Points:

- Global Positioning System captured crustal deformation during 27 hours between the 2014 Iquique mainshock and its largest aftershock
- The afterslip area south of the mainshock area impeded the mainshock rupture, preventing simultaneous occurrence of the largest aftershock
- The interevent afterslip is accompanied by accelerating seismicity, exhibiting nucleation of the largest aftershock driven by afterslip

Abstract (<= 150 words)

Various earthquake models predict that aseismic slip modulates the seismic rupture process but observations of such aseismic slip are scarce. We analyze seismic and aseismic processes during the 2014 Iquique earthquake sequence. High-rate Global Positioning System (GPS) coordinates demonstrate that afterslip started immediately after the M 8.1 mainshock. Most of the interevent afterslip is located downdip of the mainshock and is accompanied by aftershocks, both of which rapidly decay with time. An intriguing secondary afterslip peak separates the mainshock rupture from its M 7.6 largest aftershock, located ~120 km further south. This interevent afterslip area likely acted as a barrier to the southward propagation of the mainshock rupture and delayed the largest aftershock occurrence. Seismicity accelerates in this area during the 27-hour interevent stage, suggesting that the largest aftershock nucleation was driven by the interevent afterslip. Therefore, the mechanical connection between sequential great earthquakes can be mediated by afterslip.

Plain Language Summary

Subduction zone faults host both fast (regular earthquakes, seismic) and slow (aseismic) slip. Simulation models predict that slow slip can affect fast slip processes. We explored such an interaction taking place during the 2014 Iquique earthquake offshore northern Chile using observation data of crustal deformation by GPS and earthquakes. We discovered that the fast mainshock slip was terminated by a slowly slipping fault zone, which prevented the simultaneous occurrence of the largest aftershock. Furthermore, afterslip, one type of slow slip following the mainshock helped the occurrence of the largest aftershock 27 hours after the mainshock. Therefore, the sequential occurrence of large earthquakes is controlled by slowly slipping faults.

1 Introduction

Subduction zone megathrust faults host diverse slip behaviors. Seismic and aseismic slip are two complementary types (e.g., Scholz, 1998). Laboratory experiments and mechanical numerical simulations of earthquake sources demonstrate that aseismic and seismic processes commonly interact with each other in various manners. Such seismic and aseismic interaction processes are often observed associated with large earthquakes as well. For example, the nucleation of earthquakes are associated with precursory seismic and aseismic processes (e.g., Cattania & Segall, 2021; Dieterich, 1992; McLaskey, 2019; Noda et al., 2013). Short-term (a few days; e.g., Kato et al., 2012, Ohta et al., 2012) and long-term (a few months to a decade; e.g., Marill et al., 2021; Mavrommatis et al., 2014) changes in GPS coordinate series and seismic activity before the 2011 Tohoku earthquake have been interpreted in this regard. In addition, seismic ruptures are often terminated by an aseismic segment (e.g., model; Kaneko et al., 2010; the 2011 M_w 9.0 Tohoku earthquake, Nishikawa et al., 2019 and the 2007 M_w 8.0 Pisco earthquake; Perfettini et al., 2010; the 2016 M_w 7.8 Pedernales earthquake; Rolandone et al., 2018). Finally, laboratory earthquakes can interact via migrating aseismic creep fronts, and thus be responsible for the delayed triggering of laboratory earthquakes (e.g., Cebry et al., 2022). In nature, aftershock occurrence is often controlled by afterslip (the 2020 M_w 6.9 Atacama earthquake, Klein et al., 2021; the 2015 M_w 8.3 Illapel earthquakes, Perfettini et al., 2018). These

theoretical and observational studies suggest that mechanically heterogeneous faults yield various scenarios of seismic-aseismic interactions.

The 2014 M 8.1 Iquique earthquake in northern Chile along the Nazca megathrust (Figure 1a) is also an excellent target for studying such seismic-aseismic interaction in nature. Long-term locking models illustrate a heterogeneous mosaic of locked and creeping areas (Jolivet et al., 2020; Li et al., 2015; Métois et al., 2016). The 2014 event was preceded by short- (2-3 weeks) and long-term (8 months to years) precursory seismic and aseismic activities in and around the subsequent mainshock rupture area (Boudin et al., 2022; Kato et al., 2016; Ruiz et al., 2014; Schurr et al., 2014; Socquet et al., 2017; Twardzik et al., 2022). Despite these previous studies, interevent processes between the 2014 mainshock and the largest aftershock (M 7.6, Figure 1a) have so far remained unstudied. This largest aftershock occurred ~120 km south of the mainshock (Duputel et al., 2015; Hayes et al. 2014; Jara et al., 2018; Meng et al., 2015; Ruiz et al., 2014) and is delayed by 27 hours. Resolving aseismic processes at such a short time scale is usually challenging because it requires subdaily GPS coordinates, which are much noisier than those of standard daily coordinates. However, outcomes of their applications to document early postseismic processes (e.g., Jiang et al., 2021; Miyazaki & Larson, 2008; Tsang et al., 2019, Periollat et al. 2022) encourage us to investigate the interevent signals.

This study investigates source processes during the 2014 Iquique sequence and their implications for earthquake mechanics by unveiling the interevent aseismic slip using high-rate GPS and comparing them with seismicity. Our interevent aseismic slip is then juxtaposed with the location of aseismic slip during the long precursory phase, the afterslip following the largest aftershock, and the interseismic long-term locking. From this comparison, we discuss the regional aseismic modulation of rupture segmentation controlled by mechanically heterogeneous megathrust at various temporal scales. We further discuss the role of the interevent aseismic slip in the triggering and nucleation of the largest aftershock and gain insights into the aseismic mediation of sequential great earthquake occurrence.

2 Methods

2.1 High-rate GPS data analysis

2.1.1 GPS data cleaning

We employed 5-minute high-rate GPS coordinates processed by Nevada Geodetic Laboratory (Blewitt et al., 2018; black in Figure S1) (See Text S1 for details). We removed coordinate fluctuations due to multipath (e.g., Bock et al., 2000; Itoh & Aoki, 2022; Ragheb et al., 2007) and diurnal variations using Seasonal-Trend decomposition using LOESS (STL) (Cleveland et al., 1990) with a repeating period of 86100 and 86400 seconds, respectively (red and pink in Figure S1) from 5-minute coordinates. Then, we removed common mode errors originating from the fluctuation of the reference frame and satellite orbit errors (Wdowinski et al., 1997). We extracted common mode errors by stacking cleaned and despiked time series at 6 sites in the nodal direction of the mainshock and the largest aftershock, where little coseismic deformation is expected (Figure 1 and orange in Figure S1).

2.1.2 Trajectory model for cumulative displacements

To extract crustal deformation of the mainshock, the interevent stage, the largest aftershock, and the subsequent postseismic stage (2 days), we fit a trajectory model (Figures 1c-e, S2a-c) to the cleaned GPS data (blue in Figure S1) between 5 days before and 30 days after the day of the mainshock. Our trajectory model $x(t)$ is

$$x(t) = a + \left\{b + c \log\left(1 + \frac{t-t_0}{d}\right)\right\} H(t - t_0) + \left\{e + f \log\left(1 + \frac{t-t_1}{g}\right)\right\} H(t - t_1) \quad (1)$$

where *a, b,* and *e* are the initial position and coseismic offsets of the mainshock (at time $t = t_0$) and the largest aftershock (at $t = t_1$), respectively. The first and second logarithmic terms model postseismic responses assuming velocity-strengthening afterslip (Marone et al., 1991; Perfettini & Avouac, 2004; Perfettini et al., 2018) induced by the mainshock and the largest aftershock, respectively. We attempted to fit different functions (Marill et al., 2021; Periollat et al., 2022), but the fluctuations left did not allow us to significantly distinguish them. We determined the time constant(s) of the logarithmic term(s) and the other parameters by grid search and the least square regression, respectively. The search range for *d* and *g* is 0.1 – 3 and 0.1 – 10 days, respectively. For sites north of 19°S, we excluded the term relating to the largest aftershock (i.e., the third term of Equation (2)) and set the search range for *d* as 0.1 – 10 days by considering the largest aftershock size and the great hypocenter distance.

We applied this trajectory model to fit the cleaned time series twice to mitigate outlier effects (See Text S2 for details). We retrieved surface deformation at the four stages from the trajectory model fit result (Figures 1c-e, S2a-c, and S3a-f). Coseismic displacements of the two quakes (Figures S3a-b and S3d-e) are adopted from the amplitudes of step terms (i.e., *b* and *e*) while displacements during the two aseismic stages are increments of the model prediction (Figures 1b, S2d, S3c, and S3f). The derivation of formal displacement errors is explained in Text S2.

We do not discuss the temporal evolution process with this trajectory model fit result because the time constants are poorly constrained due to the noise left in the cleaned data and the short duration of interevent stage (Figure S4). Instead, we use motograms to discuss the interevent deformation evolution as described in the next section.

2.1.3 Motogram analysis for interevent deformation evolution

We computed the moving median of the cleaned GPS coordinates with a window length of 0.5 days (Figure 2a; see Text S3 for details). This approach keeps more information from the original observations than the trajectory model outputs with poorly constrained time constants (Figure S4). We derived the other dataset of the cumulative interevent displacements (Figures S5a-b) and their incremental displacements during the first and the last halves (Figures 2e-f and S5c-d) from the obtained moving average.

2.2 Slip inversions

We performed slip inversion using a non-linear slip inversion code SDM (Wang et al., 2009) to infer slip distribution during the two earthquakes and the two aseismic stages. This allows us to depict the interplay of seismic and aseismic slip in a methodologically consistent

manner, although many other models were already published except for the interevent stage (Boudin et al., 2022; Duputel et al., 2015; Hayes et al. 2014; Jara et al., 2018; Meng et al., 2015; Ruiz et al., 2014). We inverted the three components of GPS displacements weighted according to their formal errors (See also Text S4 for details of interevent datasets). We used the homogeneous isotropic elastic half-space (Okada, 1992) and fault geometry following Slab2 (Figure 1a; Hayes, 2018). We imposed a slip roughness constraint to regularize the inversion problem and we determine its strength based on a trade-off curve of data misfit versus slip roughness (Figure S6-S7). We constrain the rake angle to be between 45 and 135 degrees. We used 30 GPa for rigidity to compute seismic moment and Coulomb Stress Change (CSC; King et al. 1994; Figure S8).

For the incremental slip during the first and second halves of the interevent stage (Figure 2e-f), we found it necessary to additionally constrain the upper bound of slip (Text S4) because the incremental displacements derived from the motogram analysis are noisier.

2.3 Seismicity analysis

We employed a machine-learning-based catalog which lists many moderate aftershocks (McBrearty et al., 2019) (Figures 1b, 2e-g, and 3a) among available catalogs (Sippl et al., 2018; Soto et al., 2019). We carried out analyses of seismicity count (Figure 2c) and moment (Figure 2d) for two regions. We divided the studied region at 20.2°S within a range from 71.5°W to 70.0°W to highlight the contrast in moderate seismicity in the mainshock and the largest aftershock areas. We composed and then normalized the cumulative event count and seismicity moment with a 0.002-day window. We defined the seismicity moment of each event as $10^{1.5M_L}$ where M_L is the local magnitude supplied in the catalog. We interpret only the normalized curves because they exactly match the seismic moment evolution if $M_L = M_w + const$ holds (e.g., Hanks & Kanamori, 1979).

3 Results

3.1 Cumulative GPS displacements and slip distributions at each stage

Our cleaned time series, as well as the static cumulative displacements at each co- and post-seismic stage, demonstrate a coherent trenchward displacement pattern (Figure 1). Such postseismic displacements are compatible with the occurrence of afterslip (Hoffmann et al., 2018; Shrivastava et al., 2019). Two-day postseismic displacements following the largest aftershock similarly indicate trenchward motion but with a different spatial pattern; the largest displacement is observed near the epicenter of the largest aftershock (Figures 1 and S3c).

The imaged interevent cumulative afterslip has two peaks (blue contours in Figures 3a and S2e). The largest afterslip peak is located down-dip of the mainshock slip, a typical feature due to the depth-dependent change in megathrust rheology (e.g., Scholz, 1998). The other resolved afterslip peak is located south of the mainshock slip peak, at a seismogenic depth with moderate seismicity. This peak of slip is supported by displacements recorded at coastal sites at ~20.2°S (Figure S9) hence not artifacts. A smoother solution shows a less notable peak between the two epicenters with larger residuals at the nearest sites (Figure S6b), again highlighting the necessity of the south slip peak. The two-day afterslip following the largest aftershock is also

located close to these two peaks with different amplitudes; the slip is larger in the southern region close to the largest aftershock (Figures 3 and S3i).

3.2 Temporal evolution of interevent deformation and slip

Motograms of the smoothed time series display coherent trenchward motion, concordant at the first order with the trajectory model fit (Figures 1b and 2a). The geodetic slip during the first and second half of the interevent stage, inferred from the motograms, indicates similar patterns as the cumulative slip (Figures 2e-f, 3a, and S5). These motograms highlight the emergence of interevent deformation right after the mainshock occurrence and their subsequent steady decay. Hence, a substantial portion of the inferred geodetic slip is afterslip.

Coastal sites near the southern interevent afterslip area show a southward deflection of the motion during the late interevent stage, starting ~15 hours after the mainshock (Figure 2a), illustrated also in displacement fields of the first and second halves (Figures 2e-f). The motion of sites near the mainshock decays more rapidly than sites at the largest aftershock latitude (Figure 2a). These features suggest a temporal change in the slip pattern or perhaps a small part of the aseismic slip migrated southward.

3.3 Seismicity evolution at the mainshock and the largest aftershock area

Contrary to the geodetic data analysis, the evolution of moderate seismicity notably indicates the contrast in the mainshock and the largest aftershock areas (Figures 2c-d). In the northern mainshock area, the moment evolution inferred from seismicity shows very rapid decay because most of the larger events occurred during the first stage. In contrast, in the southern largest aftershock area, the geodetic slip decays over time while the seismicity rate increases with time. Furthermore, an increase of moment release is intermittent and dominated by the M 6.1 event that occurs 45 minutes before the interevent stage (Figure 2f-g). These seismicity events do not exhibit obvious southward migration, although aftershock migration is typical following great earthquakes and is possibly driven by afterslip (Klein et al., 2021, Perfettini et al., 2018).

4 Discussion and Conclusions

4.1 Along-strike megathrust heterogeneity and rupture segmentation

The inferred peak slip of the largest aftershock overlaps with the interevent and the largest-aftershock afterslips (Figure 3), in contradiction with the basic consensus about fault slip modes from rate and state friction law (e.g., Scholz, 1998) and some observations (Nishikawa et al., 2019; Perfettini et al., 2010; Rolandone et al., 2018). The aseismic and seismic moment maxima are slightly shifted (Figure 3b). Models with different roughness provide insights into robust slip features and, in particular, rougher solutions perhaps highlight the “minimum” extent of the slipping area (Figures S6-S7). One of the rougher solutions of the interevent aseismic slip demonstrates that the off-Iquique afterslip area split into two; one of them is located away from

the largest aftershock slip area (Figure S6c). Hence, we believe that the overlap of seismic and aseismic slip offshore Iquique might not be as substantial as seen in our preferred solution.

The interevent afterslip area south of the mainshock likely acted as a barrier to the southward propagation of the mainshock rupture (Duputel et al., 2015; Hayes et al. 2014; Jara et al., 2018; Meng et al., 2015) (Figures 3 and 4b) and prevented the immediate occurrence of the largest aftershock despite a positive mainshock CSC at the largest aftershock epicenter (Fig. S8a). This aseismic barrier was proposed from an afterslip since the largest aftershock (Shrivastava et al., 2019), and our interevent afterslip unambiguously confirms it. Similarly, other megathrust earthquakes such as the 2003 Tokachi-oki and the 2020 Atacama earthquake sequences have involved spatiotemporally close large earthquake sequences and interevent afterslip (Klein et al., 2021; Miyazaki & Larson, 2008). These examples and our findings indicate that the local mosaic of seismic and aseismic slip patches plays an important role in controlling the sequential activity of large megathrust earthquakes.

Furthermore, the megathrust off-Iquique has been creeping at different stages of the seismic cycle (Fig. 4a). The afterslip lasted there at least for over 9 months (Shrivastava et al., 2019). Different long-term interseismic locking models agree with the tendency of lower degrees of locking than the neighbor sections to the south and north (Figure 4b; Jolivet et al., 2020; Li et al., 2015; Métois et al., 2016). The pre-mainshock aseismic transient over 8 months (black contours in Figs. 3A-B; Socquet et al., 2017) overlaps with these aseismic slip regions. Such creeping megathrust could be understood as a zone of velocity-strengthening friction (Perfettini & Avouac, 2004). However, off-Iquique is not located at the controversial border of the 1868 Mw 8.8 and the 1877 Mw 8.5 ruptures but within the 1877 M_w 8.5 segment (Figures 1a, 4, and S10) (Comte & Pardo, 1991; Kausel, 1986). Hence, even with such an aseismic behavior, the interevent afterslip area off-Iquique is not a permanent barrier but can be broken during larger earthquakes (Kaneko et al., 2010). In contrast, we speculate that the area north of the mainshock hosting the interevent afterslip and the largest aftershock is a persistent aseismic barrier because it coincides with the possible end of the 1877 rupture (Figure 1a). Another afterslip peak overlapping with the 8-month pre-mainshock slip peak at greater depth (Figure 4a) implies the persistent aseismic behavior controlled by ductile fault rheology (e.g., Scholz, 1998).

Mechanisms other than fault friction can also realize the mechanically heterogeneous megathrust modulating rupture processes. Faults with irregular geometry favor creep more than large earthquakes (Wang & Bilek 2011). Off-Iquique, along-strike change in gravity anomaly (Maksymowicz et al., 2018; Molina et al., 2021), subparallel fault distribution along the megathrust (Cubas et al., 2022), seamounts on the megathrust interface (Geersen et al., 2015), and Iquique ridge on the incoming Nazca plate have been reported (Figures 1a and S10). They imply that the off-Iquique megathrust is more heterogeneous than the neighbor segments along-strike and are consistent with the presence of the aseismic megathrust. At the north of the mainshock latitude, excess fluid pressure along the megathrust may prevent the accumulation of elastic strain (Ma et al., 2022), which might explain the persistent barrier there.

4.2 Evolution of seismic-aseismic interaction toward the largest aftershock

The off-Iquique interevent afterslip area is accompanied by moderate seismicity. They exhibit the increase of occurrence rate toward the largest aftershock with their intermittent

moment release (Figures 2c-d and 2g). Notably, an M 6.1 event occurred close to the largest aftershock epicenter (~32 km) just 45 minutes before the largest aftershock (Soto et al., 2019). We interpret these seismicity characteristics as an indication of a cascade-up process during the largest aftershock nucleation (e.g., Ellsworth & Bulut, 2018; Kato & Ben-Zion, 2021; McLaskey, 2019). Although this nucleation scenario does not require aseismic slip, aseismic slip can cause the occurrence of moderate seismicity. The rate-dependent cascade-up model describing such a mixed-mode nucleation (Kato & Ben-Zion, 2021; McLaskey, 2019) better explains our observations. However, numerical models usually demonstrate the acceleration of precursor aseismic slip (e.g., Cattania & Segall, 2021; Dieterich, 1992; Noda et al., 2013), which our high-rate GPS series do not suggest. Hence, our interevent geodetic slip is less likely a part of the largest aftershock nucleation but brought instability to the largest aftershock fault by loading stress, having started before the mainshock (Figure 4; Socquet et al., 2017). The negative CSC due to the interevent slip in the largest aftershock epicentral area probably reflects a cumulative stress drop associated with the nucleation (Figure S8b). Instantaneous stress loading during the interevent stage due to the cascading seismicity should have a much shorter spatial wavelength and hence the contribution of these moderate earthquakes is smeared out in the slip inversion. Actually, the stress perturbation brought by the interevent aseismic slip is much smaller than the mainshock (Figure S8), but those values depend largely on the inversion protocol, particularly, the strength of the roughness constraint, so we only interpret the sign of CSC here. More quantitative discussion is beyond the scope of this observational paper.

Similar scenarios to our observation-based findings are found in some numerical simulations. Cattania and Segall (2021) demonstrated feedback of aseismic and seismic precursors in the geometrically rough fault. A fault model with hierarchical frictional parameters demonstrated that afterslip in the subsequent rupture area sometimes prompts it by reducing the strength (Noda et al., 2013). Given the possible complex structure off-Iquique (Figure S10), a comparison of our models and these simulations may highlight the importance of frictional and geometrical heterogeneity of faults.

Another intriguing question relates to the delayed occurrence of the largest aftershock. After the mainshock rupture was impeded, the afterslip emerged, but it did not immediately trigger the largest aftershock. Such delay might be controlled by migrating slow slip (Ariyoshi et al., 2019; Cebry et al., 2022), but our high-rate GPS observations and seismicity pattern did not support interevent aseismic slip migration as the dominant process.

4.3 Observational perspective

Observational evidence of interevent afterslip leading to large megathrust earthquakes is limited to the 2011 Tohoku (51 hours; Ohta et al., 2012) and 2014 Iquique cases. The careful re-examination of GPS data utilizing high-rate processing would probably discover more examples of inter-large-event aseismic processes. However, our interpretation regarding the 2014 case still contains large uncertainty due to the limited number of sites and the large data uncertainty, which did not allow us to investigate more quantitative mechanical links among the slips at the different stages. The improvement of noise reduction techniques is inevitable for significantly improving our understanding of earthquake mechanics.

Acknowledgments
The authors declare no conflicts of interest. This study is supported by Japan Society for the Promotion of Science (JSPS) Overseas Research Fellowships and KAKENHI 21K14007 (YI) and ERC CoG 865963 DEEP-trigger (AS). Discussion with Jorge Jara, Zaccaria El Yousfi, Michel Bouchon, Satoshi Ide, Jean-Philippe Avouac, and Sylvain Barbot was fruitful. Nadaya Cubas provided us with results of Cubas et al. (2022). English check of an earlier version manuscript by James Hollingsworth helped improve the manuscript. Y.I. is a Japan Society for the Promotion of Science (JSPS) Overseas Research Fellow.

Open Research
We processed only publicly available data. The GPS coordinates (Blewitt et al., 2018) are available at http://geodesy.unr.edu/. The seismicity catalog of Soto et al. (2019) is available at https://datapub.gfz-potsdam.de/download/10.5880.GFZ.4.1.2019.009/Iquique_earthquake_seismicity_catalogue_2014.txt. The gravity anomaly (Sandwell et al., 2014) and topography (Smith & Sandwell, 1997) data are available at https://topex.ucsd.edu/cgi-bin/get_data.cgi. The inversion code SDM (Wang et al., 2009) is available at https://gfzpublic.gfz-potsdam.de/pubman/item/item_1975902. We made our slip distribution of the interevent afterslip available in xxx (ready at publication).

References

Ariyoshi, K., Ampuero, J. P., Bürgmann, R., Matsuzawa, T., Hasegawa, A., Hino, R., & Hori, T. (2019). Quantitative relationship between aseismic slip propagation speed and frictional properties. *Tectonophysics*, 767, 128151. https://doi.org/10.1016/j.tecto.2019.06.021

Blewitt, G., Hammond, W. C., & Kreemer, C. (2018). Harnessing the GPS data explosion for interdisciplinary science. *Eos, 99.* https://doi.org/10.1029/2018EO104623

Bock, Y., Nikolaidis, R. M., de Jonge, P. J., & Bevis, M. (2000). Instantaneous geodetic positioning at medium distances with the Global Positioning System. *Journal of Geophysical Research: Solid Earth* 105, 28223–28253. https://doi.org/10.1029/2000JB900268

Boudin, F., et al. (2022). Slow slip events precursory to the 2014 Iquique Earthquake, revisited with long-base tilt and GPS records, *Geophysical Journal International* 228, 2092–2121. https://doi.org/10.1093/gji/ggab425

Caballero, E., Chounet, A., Duputel, Z., Jara, J., Twardzik, C., & Jolivet, R. (2021). Seismic and aseismic fault slip during the initiation phase of the 2017 M_W = 6.9 Valparaíso earthquake. *Geophysical Research Letters*, 48, e2020GL091916. https://doi.org/10.1029/2020GL091916

Cattania, C., & Segall, P. (2021). Precursory slow slip and foreshocks on rough faults. *Journal of Geophysical Research: Solid Earth* 126, e2020JB020430. https://doi.org/10.1029/2020JB020430

Cebry, S. B. L., Ke, C. Y., Shreedharan, S. Marone, C., Kammer, D. S., McLaskey, G. C. (2022). Creep fronts and complexity in laboratory earthquake sequences illuminate delayed earthquake triggering. *Nature Communications*, 13, 6839. https://doi.org/10.1038/s41467-022-34397-0

Cleveland, R. B., Cleveland, W. S., McRae, J. E., & Terpenning, I. (1990). STL: A seasonal-trend decomposition procedure based on loess. *Journal of Official Statistics,* 6, 3–73

Comte, D., & Pardo, M. (1991). Reappraisal of great historical earthquakes in the northern Chile and southern Peru seismic gaps. *Natural Hazards*, 4, 23–44. https://doi.org/10.1007/BF00126557

Cubas, N., Agard, P., & Tissandier, R. (2022). Earthquake ruptures and topography of the Chilean margin controlled by plate interface deformation. *Solid Earth* 13, 779–792. https://doi.org/10.5194/se-13-779-2022

DeMets, C., Gordon, R. G., & Argus, D. F.(2010). Geologically current plate motions. *Geophysical Journal International,* 181, 1–80. https://doi.org/10.1111/j.1365-246X.2009.04491.x

Dieterich, J. H. (1992). Earthquake nucleation on faults with rate-and state-dependent strength. *Tectonophysics*, 211, 115-134. https://doi.org/10.1016/0040-1951(92)90055-B

Duputel, Z., et al. (2015). The Iquique earthquake sequence of April 2014: Bayesian modeling accounting for prediction uncertainty, *Geophysical Research Letter,s* 42, 7949–7957. https://doi.org/10.1002/2015GL065402

Ellsworth, W. L., & Bulut, F. (2018). Nucleation of the 1999 Izmit earthquake by a triggered cascade of foreshocks. *Nature Geoscience,* 11, 531–535. https://doi.org/10.1038/s41561-018-0145-1

Geersen, J., Ranero, C., Barckhausen, U., & Reichert, C. (2015), Subducting seamounts control interplate coupling and seismic rupture in the 2014 Iquique earthquake area. *Nature Communications,* 6, 8267. https://doi.org/10.1038/ncomms9267

Hanks, T. C., & Kanamori, H. (1979). A moment magnitude scale, *Journal of Geophysical Research: Solid Earth*, 84, 2348– 2350. https://doi.org/10.1029/JB084iB05p02348

Hayes, G. (2018). Slab2 - A comprehensive subduction zone geometry model. *U.S. Geological Survey data release*.

Hayes, G., et al. (2014). Continuing megathrust earthquake potential in Chile after the 2014 Iquique earthquake. *Nature,* 512, 295–298. https://doi.org/10.1038/nature13677

Hoffmann, F., Metzger, S., Moreno, M., Deng, Z., Sippl, C., Ortega-Culaciati, F., & Oncken, O. (2018). Characterizing afterslip and ground displacement rate increase following the 2014 Iquique-Pisagua M_w 8.1 earthquake, Northern Chile. *Journal of Geophysical Research: Solid Earth*, 123, 4171–4192. https://doi.org/10.1002/2017JB014970

Ito, Y., et al. (2013). Episodic slow slip events in the Japan subduction zone before the 2011 Tohoku-Oki earthquake. *Tectonophysics*, 600, 14-26. https://doi.org/10.1016/j.tecto.2012.08.022

Itoh, Y., & Aoki, Y. (2022). On the performance of position-domain sidereal filter for 30-s kinematic GPS to mitigate multipath errors. *Earth, Planets and Space,* 74, 23. https://doi.org/10.1186/s40623-022-01584-8

Jara, J., et al. (2018). Kinematic study of Iquique 2014 Mw 8.1 earthquake: Understanding the segmentation of the seismogenic zone. *Earth and Planetary Science Letters,* 503, 131-143. https://doi.org/10.1016/j.epsl.2018.09.025

Jiang, J., Klein, E., & Bock, Y. (2021). Coevolving early afterslip and aftershock signatures of a San Andreas fault rupture. *Science Advances*, 7, eabc1606 https://doi.org/10.1126/sciadv.abc1606

Jolivet, R., Simons, M., Duputel, Z., Olive, J.-A., Bhat, H. S., & Bletery, Q. (2020). Interseismic loading of subduction megathrust drives long-term uplift in Northern Chile. *Geophysical Research Letters,* 47, e2019GL085377. https://doi.org/10.1029/2019GL085377

Kaneko, Y., Avouac, J.-P. & Lapusta, N. (2010). Towards inferring earthquake patterns from geodetic observations of interseismic coupling. *Nature Geosciences,* 3, 363–369. https://doi.org/10.1038/ngeo843

Kato, A., & Ben-Zion, Y. (2021). The generation of large earthquakes. *Nature Reviews Earth & Environment* 2, 26–39. https://doi.org/10.1038/s43017-020-00108-w

Kausel, E. (1986). Los terremotos de agosto de 1868 y mayo de 1877 que afectaron el sur del Perú y norte de Chile. Boletín de la Academia Chilena de Ciencias 3, 8–13

Kato, A., Fukuda, J., Kumazawa, T., & Nakagawa, S. (2016). Accelerated nucleation of the 2014 Iquique, Chile Mw 8.2 Earthquake. *Scientific Reports,* 6, 24792 https://doi.org/10.1038/srep24792

Kato, A., Obara, K., Igarashi, T., Tsuruoka, H., Nakagawa, S., & Hirata, N. (2012) Propagation of Slow Slip Leading Up to the 2011 M_w 9.0 Tohoku-Oki Earthquake. *Science* 335, 705-708. https://doi.org/10.1126/science.1215141

King, G. C. P., Stein, S. S., Lin, J. (1994). Static stress changes and the triggering of earthquakes. *Bulletin of Seismological Society of America.* 84, 935–953. https://doi.org/10.1785/BSSA0840030935

Klein, E. (2021). Interplay of seismic and a-seismic deformation during the 2020 sequence of Atacama, Chile. *Earth and Planetary Science Letters* 570, 117081. https://doi.org/10.1016/j.epsl.2021.117081

Li, S., Moreno, M., Bedford, J., Rosenau, M., Oncken, O. (2015). Revisiting viscoelastic effects on interseismic deformation and locking degree: A case study of the Peru-North Chile subduction zone. *Journal of Geophysical Research: Solid Earth* 120, 4522–4538. https://doi.org/10.1002/2015JB011903

Ma, B., et al., (2022). Megathrust reflectivity reveals the updip limit of the 2014 Iquique earthquake rupture. *Nature Communications* 13, 3969. https://doi.org/10.1038/s41467-022-31448-4

Maksymowicz, A., Ruiz, J., Vera, E., Contreras-Reyes, E., Ruiz, S., Arraigada, C., Bonvalot, S., & Bascuñan, S. (2018). Heterogeneous structure of the Northern Chile marine forearc and its implications for megathrust earthquakes. *Geophysical Journal International* 215, 1080–1097. https://doi.org/10.1093/gji/ggy325

Marill, L., Marsan, D., Socquet, A., Radiguet, M., Cotte, N., & Rousset, B., (2021). Fourteen-year acceleration along the Japan Trench. *Journal of Geophysical Research: Solid Earth* 126, e2020JB021226. https://doi.org/10.1029/2020JB021226

Marone, C. J., Scholz, C. H., & Bilham, R. (1991). On the mechanics of earthquake afterslip, *Journal of Geophysical Research: Solid Earth* 96, 8441–8452. https://doi.org/10.1029/91JB00275

Mavrommatis, A. P., Segall, P., & Johnson, K. M. (2014). A decadal-scale deformation transient prior to the 2011 M_w 9.0 Tohoku-oki earthquake, *Geophysical Research Letters*, 41, 4486–4494. https://doi.org/10.1002/2014GL060139

McBrearty, I. W., Gomberg, J., Delorey, A. A., & Johnson, P. A. (2019). Earthquake Arrival Association with Backprojection and Graph Theory. *Bulletin of Seismological Society of America* 109, 2510–2531. https://doi.org/10.1785/0120190081

McLaskey, G. C. (2019). Earthquake Initiation From Laboratory Observations and Implications for Foreshocks. *Journal of Geophysical Research: Solid Earth,* 124, 12882–12904. https://doi.org/10.1029/2019JB018363

Meng, L., Huang, H., Bürgmann, R., Ampuero, J.-P., & Strader, A. (2015). Dual megathrust slip behaviors of the 2014 Iquique earthquake sequence. *Earth and Planetary Science Letters* 411, 177-187. https://doi.org/10.1016/j.epsl.2014.11.041

Métois, M., Vigny, C., & Socquet, A. (2016). Interseismic Coupling, Megathrust Earthquakes and Seismic Swarms Along the Chilean Subduction Zone (38°–18°S). *Pure and Applied Geophysics* 173, 1431–1449. https://doi.org/10.1007/s00024-016-1280-5

Miyazaki, S., & Larson, K. M. (2008). Coseismic and early postseismic slip for the 2003 Tokachi-oki earthquake sequence inferred from GPS data. *Geophysical Research Letters* 35, L04302. https://doi.org/10.1029/2007GL032309

Molina, D., Tassara, A., Abarca, R., Melnick, D., & Madella, A. (2021). Frictional segmentation of the Chilean megathrust from a multivariate analysis of geophysical, geological, and geodetic data. *Journal of Geophysical Research: Solid Earth*, 126, e2020JB020647. https://doi.org/10.1029/2020JB020647

Nishikawa, T., Matsuzawa, T., Ohta, K., Nishimura, T. & Ide, S. (2019). The slow earthquake spectrum in the Japan Trench illuminated by the S-net seafloor observatories. *Science* 365, 808-813. https://doi.org/10.1126/science.aax5618

Noda, H., Nakatani, M., & Hori, T. (2013), Large nucleation before large earthquakes is sometimes skipped due to cascade-up—Implications from a rate and state simulation of faults with hierarchical asperities, *Journal of Geophysical Research: Solid Earth*, 118, 2924– 2952. https://doi.org/10.1002/jgrb.50211

Ohta, Y., et al. (2012). Geodetic constraints on afterslip characteristics following the March 9, 2011, Sanriku-oki earthquake, Japan. *Geophysical Research Letters*, 39, L16304, https://doi.org/10.1029/2012GL052430

Okada, Y. (1992). Internal deformation due to shear and tensile faults in a half-space. *Bulletin of Seismological Society of America,* 82, 1018–1040. https://doi.org/10.1785/BSSA0820021018

Perfettini, H., & Avouac, J. P. (2004). Postseismic relaxation driven by brittle creep: A possible mechanism to reconcile geodetic measurements and the decay rate of aftershocks, application to the Chi-Chi earthquake, Taiwan. *Journal of Geophysical Research: Solid Earth*, 109, B02304. https://doi.org/10.1029/2003JB002488

Perfettini, H., et al. (2010). Seismic and aseismic slip on the Central Peru megathrust. *Nature* 465, 78–81. https://doi.org/10.1038/nature09062

Perfettini, H., Frank, W. B., Marsan, D, & Bouchon, M. (2018). A model of aftershock migration driven by afterslip. *Geophysical Research Letters,* 45, 2283– 2293. https://doi.org/10.1002/2017GL076287

Periollat, A., Radiguet, M., Weiss, J., Twardzik, C., Amitrano, D., Cotte, N., Marill, L., & Socquet, A. (2022). Transient brittle creep mechanism explains early postseismic phase of the 2011 Tohoku-Oki megathrust earthquake: Observations by high-rate GPS solutions. *Journal of Geophysical Research: Solid Earth,* 127, e2022JB024005. https://doi.org/10.1029/2022JB024005

Ragheb, A. E., Clarke, P. J., & Edwards, S. J. (2007). GPS sidereal filtering: Coordinate- and carrier-phase-level strategies. *Journal of Geodesy,* 81, 325–335. https://doi.org/10.1007/s00190-006-0113-1

Rolandone, F., et al., (2018). Areas prone to slow slip events impede earthquake rupture propagation and promote afterslip. *Science Advances,* 4, eaao6596. https://doi.org/10.1126/sciadv.aao6596

Ruiz, S., Metois, M., Fuenzalida, A., Ruiz, J., Leyton, F., Grandin, R., Vigny, C., Madariaga, R., & Campos, J. (2014). Intense foreshocks and a slow slip event preceded the 2014 Iquique Mw 8.1 earthquake. *Science,* 345, 1165-1169. https://doi.org/10.1126/science.1256074

Sandwell, D. T., Müller, R. D., Smith, W. H. F., Garcia, E., & Francis, R. (2014). New global marine gravity model from CryoSat-2 and Jason-1 reveals buried tectonic structure. *Science*, 346, 65-67. https://doi.org/10.1126/science.1258213

Scholz, C. (1998). Earthquakes and friction laws. *Nature,* 391, 37–42. https://doi.org/10.1038/34097

Schurr, B., et al. (2014). Gradual unlocking of plate boundary controlled initiation of the 2014 Iquique earthquake. *Nature,* 512, 299–302. https://doi.org/10.1038/nature13681

Shrivastava, M. N., González, G., Moreno, M., Soto, H., Schurr, B., Salazar, P., Báez, J. C. (2019). Earthquake segmentation in northern Chile correlates with curved plate geometry. *Scientific Reports,* 9, 4403. https://doi.org/10.1038/s41598-019-40282-6

Sippl, C., Schurr, B., Asch, G., & Kummerow, J. (2018). Seismicity structure of the northern Chile forearc from >100,000 double-difference relocated hypocenters. *Journal of Geophysical Research: Solid Earth*, 123, 4063– 4087. https://doi.org/10.1002/2017JB015384

Smith, W. H. F., & Sandwell, D. T. (1997). Global seafloor topography from satellite altimetry and ship depth soundings. *Science* 277, 1957-1962. https://doi.org/10.1126/science.277.5334.1956

Socquet, A., et al. (2017). An 8 month slow slip event triggers progressive nucleation of the 2014 Chile megathrust, *Geophysical Research Letters,* 44, 4046–4053. https://doi.org/10.1002/2017GL073023

Soto, H., Sippl, C., Schurr, B., Kummerow, J., Asch, G., Tilmann, F., Comte, D., Ruiz, S., & Oncken, O. (2019). Probing the northern Chile megathrust with seismicity: the 2014 M8.1 iquique earthquake sequence. *Journal of Geophysical Research: Solid Earth,* 124, 12935–12954. https://doi.org/10.1029/2019JB017794

Tsang, L. L. H., et al. (2019). Imaging rapid early afterslip of the 2016 Pedernales earthquake, Ecuador. *Earth and Planetary Science Letters*, 524, 115724. https://doi.org/10.1016/j.epsl.2019.115724

Twardzik, C., Duputel, Z., Jolivet, R., Klein, E., & Rebischung, P. (2022). Bayesian inference on the initiation phase of the 2014 Iquique, Chile, earthquake. *Earth and Planetary Science Letters,* 600, 117835. https://doi.org/10.1016/j.epsl.2022.117835

Wang, K., & Bilek, S. L. (2011). Do subducting seamounts generate or stop large earthquakes? *Geology,* 39, 819–822. https://doi.org/10.1130/G31856.1

Wang, L., Wang, R., Roth, F., Enescu, B., Hainzl, S., & Ergintav, S. (2009). Afterslip and viscoelastic relaxation following the 1999 M 7.4 Izmit earthquake from GPS measurements, *Geophysical Journal International*, 178, 1220-1237. https://doi.org/10.1111/j.1365-246X.2009.04228.x

Wdowinski, S., Bock, Y., Zhang, J., Fang, P., Genrich, J. (1997). Southern California permanent GPS geodetic array: Spatial filtering of daily positions for estimating coseismic and postseismic displacements induced by the 1992 Landers earthquake. *Journal of Geophysical Research: Solid Earth,* 102, 18057–18070. https://doi.org/10.1029/97JB01378

References only in supporting information

Altamimi, Z., Métivier, L., Rebischung, P., Rouby, H., & Collilieux, X. (2017). ITRF2014 plate motion model. *Geophysical Journal International* 209, 1906–1912. https://doi.org/10.1093/gji/ggx136

Itoh, Y., Aoki, Y., & Fukuda, J. (2022). Imaging evolution of Cascadia slow-slip event using high-rate GPS. *Scientific Reports,* 12, 7179. https://doi.org/10.1038/s41598-022-10957-8

Pedregosa, F., et al. (2011). Scikit-learn: Machine learning in Python. *Journal of Machine Learning Research* **12**, 2825–2830.

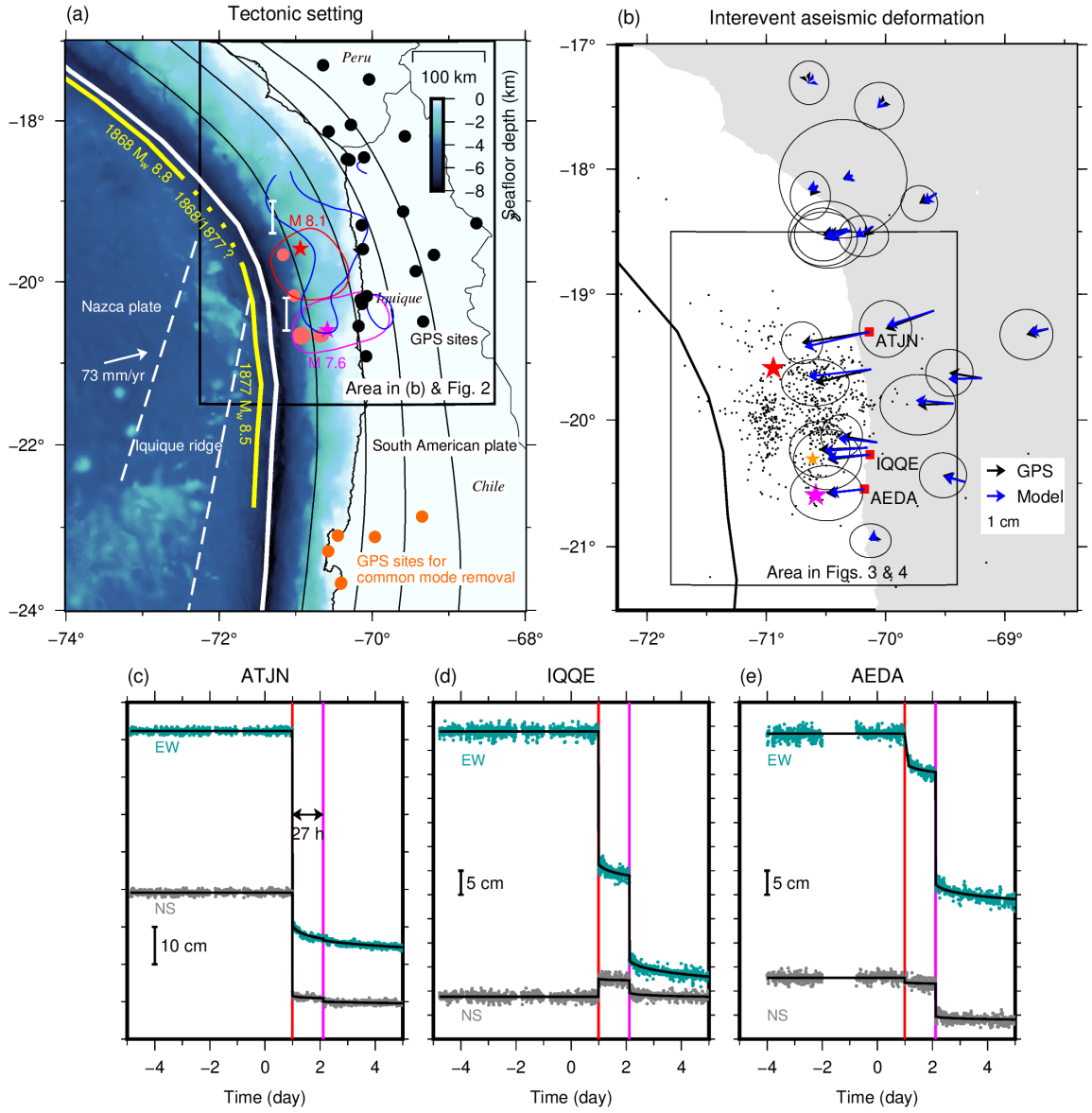

Figure 1. (a) Tectonic setting. Black dots indicate GPS sites for deformation analysis and common mode noise extraction, respectively. Red and purple stars indicate the epicenters of the 2014 Iquique mainshock and the largest aftershock, respectively (Soto et al., 2019). Red, blue, and purple curves outline slip areas of the mainshock, interevent afterslip, and the largest aftershock, respectively. A white vector indicates the plate convergence motion (DeMets et al., 2010). Slab depth is contoured at a 20-km interval from 20 km (Hayes, 2018). Yellow curves indicate rupture extension of large earthquakes with a controversial section shown as a dotted curve (Comte & Pardo, 1991; Kausel, 1986). Red ovals indicate seamounts at depth (Geersen et al., 2015). White bars offshore indicate a range of inferred aseismic barriers. (b) Interevent horizontal GPS displacements with the model prediction from slip inversion (Figure 3a). Black dots indicate interevent seismicity (McBrearty et al., 2019). (c-e) Cleaned 5-minute GPS coordinates at sites as labeled (location in (b)) with trajectory model fits (black lines). Red and pink vertical lines indicate the timings of the mainshock and the largest aftershock, respectively.

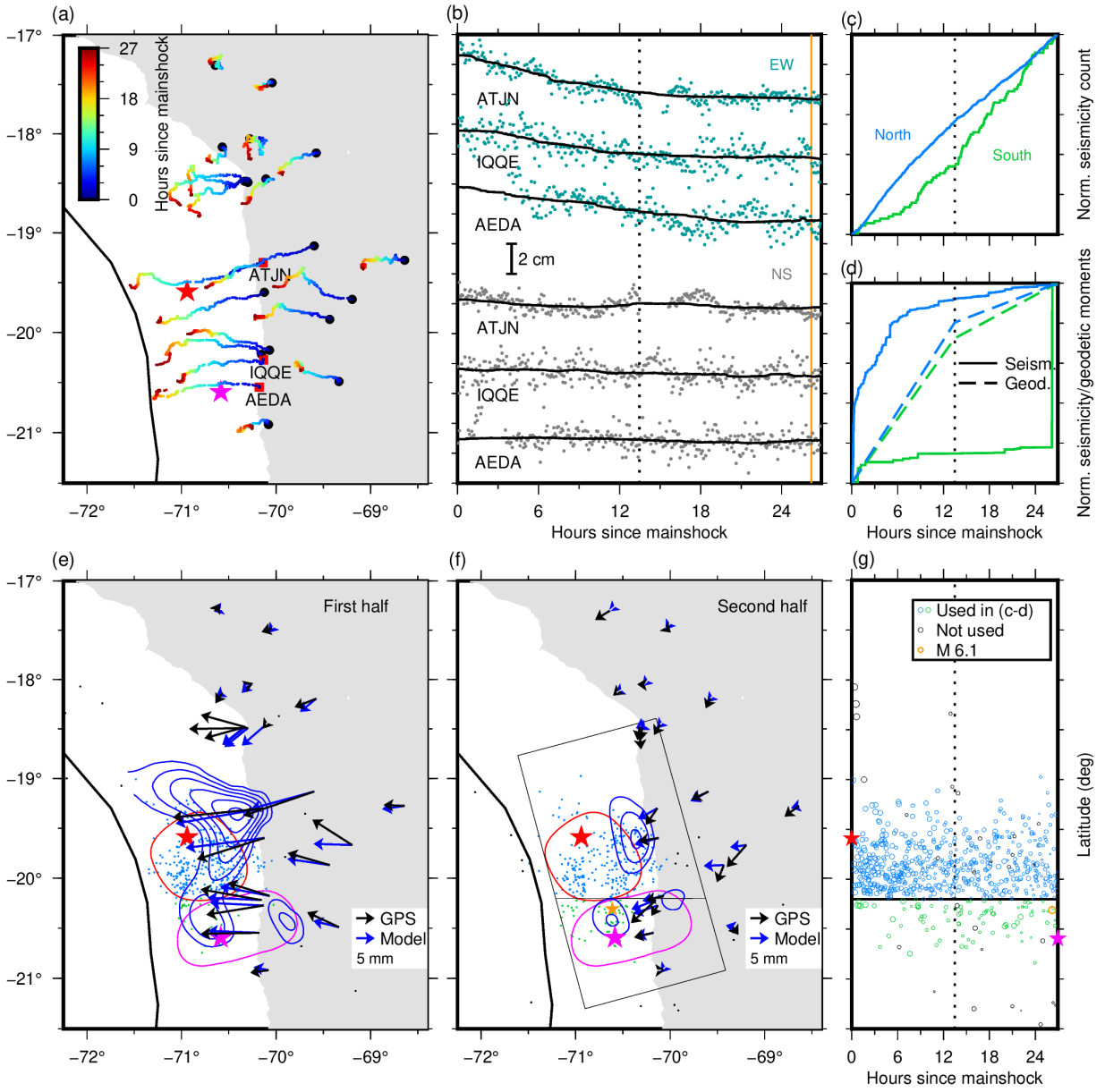

Figure 2. (a) Interevent GPS motogram. (b) Interevent GPS coordinates (dots; location in (a)) and their moving median (0.5-day window; solid lines). A dotted vertical line shows the middle point of the interevent stage. (c) Normalized seismicity count in the two regions divided at 20.2°S as labeled. Events accounted for in the calculation (McBrearty et al., 2019) are shown in (e) and (f) with corresponding colors. (d) Same as (c) but with normalized seismicity moment (solid lines). The broken lines indicate the evolution of geodetic moment (assuming a linear evolution in each window). (e-f) Interevent afterslip snapshots (4 cm interval from 4 cm) by inverting displacements from the moving median analysis (black vectors; see (b)). Error ellipses of GPS are trimmed for clarity. Displacements at sites north of 19°S are not inverted. See Figures 1 and 3 for other elements. The orange star indicates the M 6.1 epicenter (Soto et al., 2019). (g) Interevent seismicity (open circles scaled with magnitude).

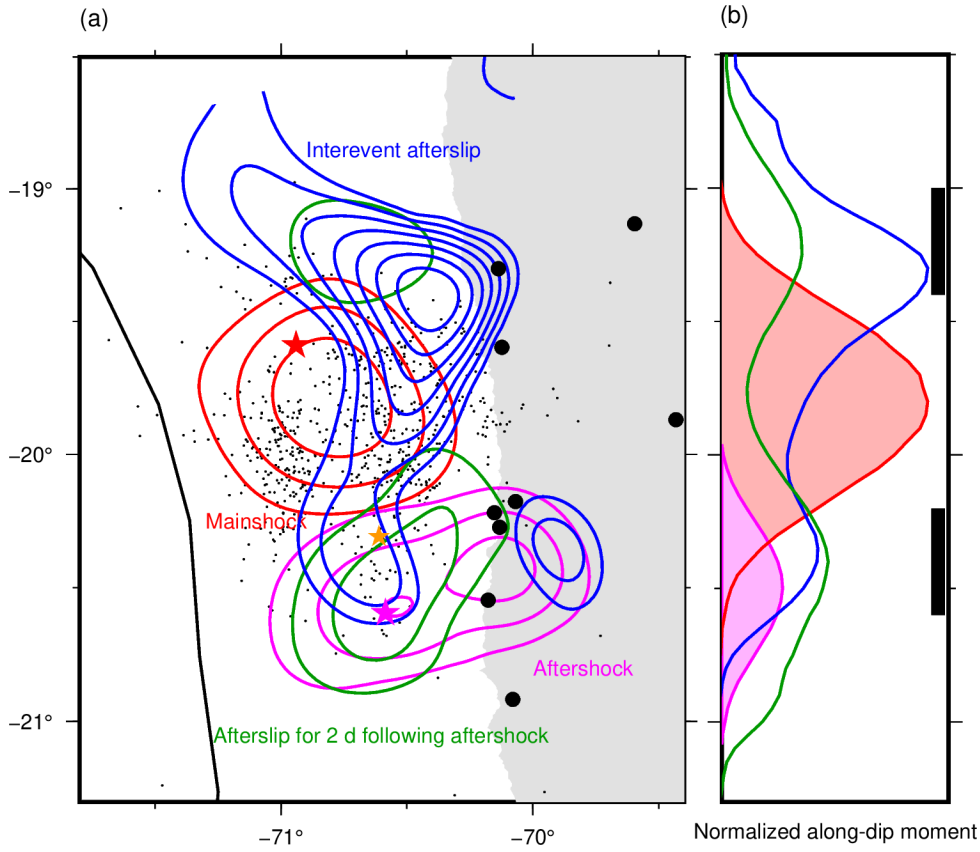

Figure 3. (a) Comparison of the mainshock coseismic slip (1-m interval from 2 m), cumulative interevent afterslip (4-cm interval from 8 cm), the largest aftershock coseismic slip (20-cm interval from 40 cm), and subsequent 2-day afterslip (4-cm interval from 8 cm) as labeled, inferred from displacements with the trajectory model fit (Figures 1c-e and S2a-c). See Figure 1 for other elements. (b) Normalized along-dip moment of each event (colors in (a)). Seismic (red and purple) and aseismic (blue and green) moments are separately normalized with respect to their maximum values (aseismic-to-seismic ratio of the normalizing factors is ~0.056). Two black bars indicate the inferred aseismic barrier location.

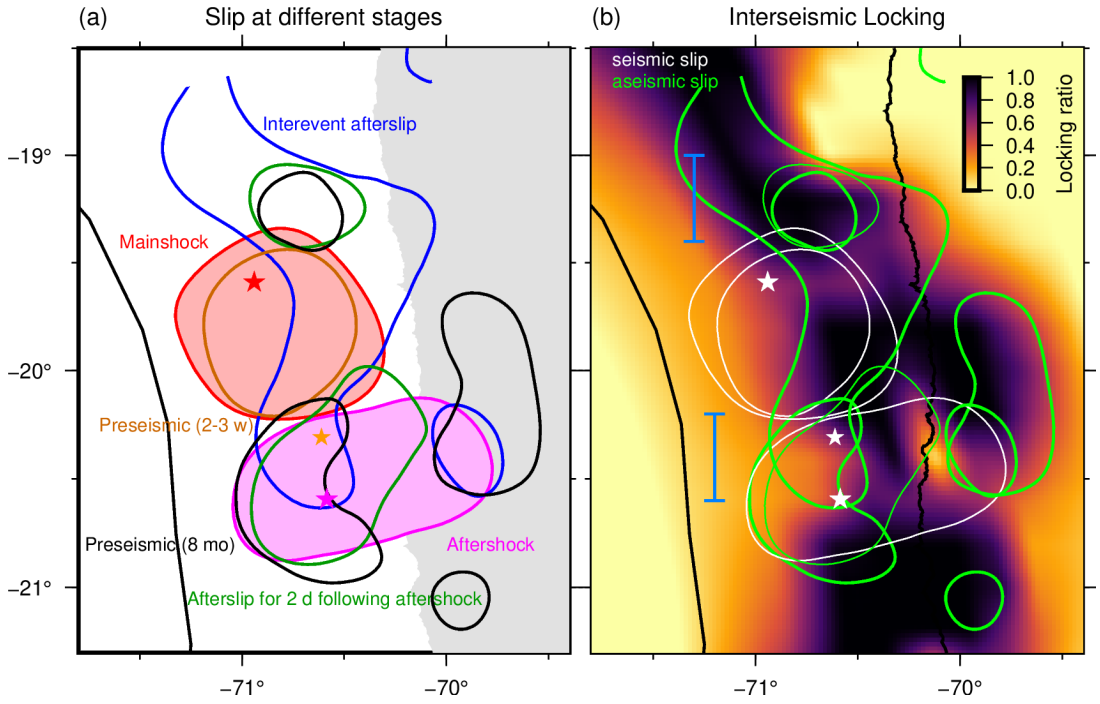

Figure 4. (a) Compilation of slips at different stages as labeled. The outmost contours in Figure 2 are drawn for events derived in this study while the two pre-mainshock contours outline 5 mm (black) and 5 cm (brown) slip (Socquet et al., 2017). (b) Same as (a) but with interseismic locking (background color) (Métois et al., 2016) and seismic (white) and aseismic (green) slip events. Preseismic (2 – 3 weeks) slip is drawn as seismic slip because ~65% of moment release was released seismically (Socquet et al., 2017). Latitudinal range of inferred aseismic barriers is shown with two light blue bars.

Geophysical Research Letters

Supporting Information for

Largest aftershock nucleation driven by afterslip during the 2014 Iquique sequence

Yuji Itoh[1,2], Anne Socquet[1], and Mathilde Radiguet[1]

[1]Univ. Grenoble Alpes, Univ. Savoie Mont Blanc, CNRS, IRD, Univ. Gustave Eiffel, ISTerre, 38000 Grenoble, France.

[2]Earthquake Research Institute, The University of Tokyo, Tokyo, Japan.

Contents of this file

Text S1. Details of GPS data cleaning

We removed spatiotemporally correlated fluctuations in 5-minute high-rate GPS coordinates processed by Nevada Geodetic Laboratory (Blewitt et al., 2018) through the following procedure. First, we fixed the GPS coordinates into the South American plate using a plate motion model with respect to ITRF2014 (Altamimi et al., 2007) (black in Figure S1). Then, we removed coordinate fluctuations due to multipath (e.g., Bock et al., 2000; Itoh & Aoki, 2022; Ragheb et al., 2007). Multipath signals are known to appear periodically, so we estimated them using Seasonal-Trend decomposition using LOESS (STL) (Cleveland et al., 1990; Pedregosa et al., 2011) which decomposes time series into trend, seasonal (i.e., periodic but non-parametric), and residual terms. Here, we chose 86100 seconds for the period because it is the integer multiple of the sampling interval closest to the typical multipath period (86154 seconds; Ragheb et al., 2007). We removed the estimated seasonal component and kept the other two terms for the subsequent analysis (red in Figure S1). Next, we removed diurnal variation in the data, using the same approach for the multipath removal but with a period of 86400 seconds (Itoh et al., 2022) (pink in Figure S1). Next, we removed common mode error which originates from the fluctuation of the reference frame and satellite orbit errors (Wdowinski et al., 1997). We extracted common mode error by stacking time series at 6 sites in the nodal direction of the

mainshock and aftershock, where little coseismic deformation is expected (Figure 1 and orange in Figure S1). Before stacking them, we removed outliers and a linear trend of time series at each site. The outliers are defined as epochs satisfying the following criterion (Equation (S1)) (Itoh et al., 2022);

$$\left|u_i - \frac{q_1+q_3}{2}\right| > n * \frac{q_3-q_1}{2} \quad \text{(S1)}$$

where, u_i is the displacement at the *i*-th epoch, q_1 and q_3 are the 25 and 75 percentile values of the position time series, respectively, derived from data between 60 days before and 30 days after the day of the mainshock. The term n is a threshold controlling how strict or loose we impose the outlier criterion and we adopted $n = 8$ in this study based on trial-and-error approaches. We estimated and removed the linear trend from the data after this outlier removal step.

Text S2. Details of the trajectory model fit procedure and error evaluation

We used Equation (1) in both of the two fitting steps, but, after the first fit, we removed outliers defined as epochs which deviate from the model prediction by 3 times post-fit RMS. RMS is here defined as

$$RMS = \sqrt{\frac{\sum_{i=1}^{n}\left(\frac{o(t_i)-x(t_i)}{w(t_i)}\right)^2}{\sum_{i=1}^{n}\frac{1}{w(t_i)^2}}} \quad \text{(S2)}$$

where, $o(t_i)$ and $w(t_i)$ are a coordinate and its error at $t = t_i$, respectively and n is the number of available epochs. Then, we again fit the same function to the data without the outliers.

For simplicity, formal displacement errors of these coseismic displacements are obtained by the linear least-square transformation of the GPS position observation errors while formal errors of the displacements at the two aseismic stages were defined as Equation (S2) except for the data length; we computed RMS with the data and the model prediction during each time window.

Text S3. Details of motogram analysis

We derived the moving median (Figures 2a-b) from the data after removing the mainshock and largest-aftershock coseismic steps estimated by the trajectory model fit. We did not exclude the pre-mainshock or post-largest-aftershock coordinates for deriving moving median values the first or last 0.25 days because, given the definition of median, distortion of the obtained moving median should be limited. Using a shorter window length by excluding these pre-mainshock or post-largest-aftershock coordinates from the calculation would have a larger impact on the results at the beginning and the end of the interevent stage.

For simplicity, formal errors of the displacements derived from the moving median (Figures 2e-f and S5) are taken from the trajectory analysis results (See Text S2).

Text S4. Inversions of incremental interevent displacements derived from the motogram analysis

For the interevent afterslip, we used four different data sets, namely, (i) the cumulative interevent displacements derived from the trajectory model fit (i.e., Equation (1); Figures 1b, 3a, and S2d-e), (ii) same as (i) but displacements derived from the moving median (Figures S5a-b), (iii) displacements during the first half of the interevent window, derived from the moving median (Figures 2e and S5c) and (iv) same as (iii) but during the second half (Figures 2f and S5d).

For inversions of the interevent afterslip with the datasets derived from the moving median analysis (i.e., Datasets (ii), (iii), and (iv); Figures 2e-f and S5), we excluded GPS sites located north of 19°S, namely those near the border of Chile and Peru, because including them highly destabilized the slip inversion. Furthermore, to obtain the consistent slip pattern in all the interevent slip models, we added a constraint to the upper bound of the slip amplitude. For the cumulative slip inversion with Dataset (ii), the upper bound is set to those obtained by the inversion of displacements obtained by the trajectory model fit (i.e., Dataset (i)). The obtained slip amplitude was

subsequently used as the upper bound of slip amplitude during the first and second halves of the interevent window with the datasets (iii) and (iv).

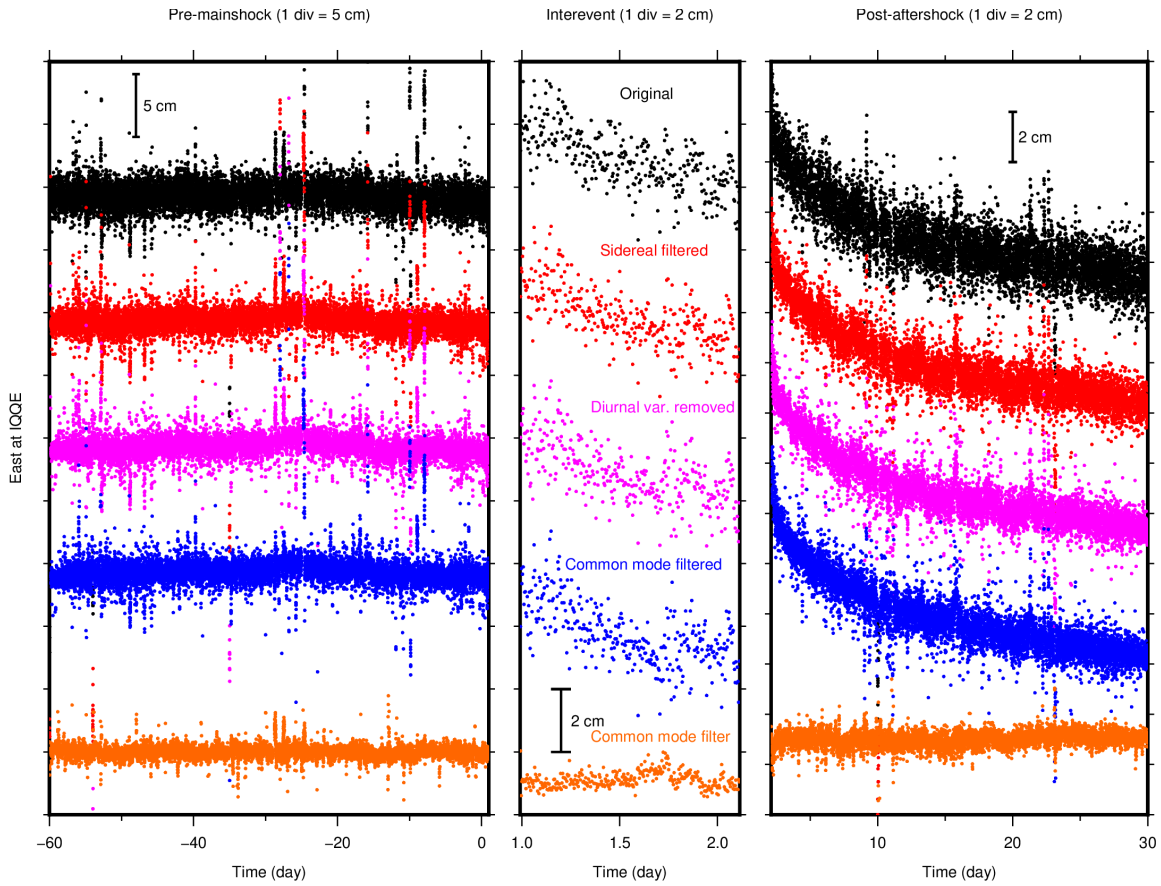

Figure S1. High-rate 5-min GPS data cleaning procedure (East component at IQQE as an example; Figure 1d). Time series with each color indicates the results of the cleaning procedure at each step as labeled. Coseismic steps of the mainshock and the largest aftershock are removed by breaking panels.

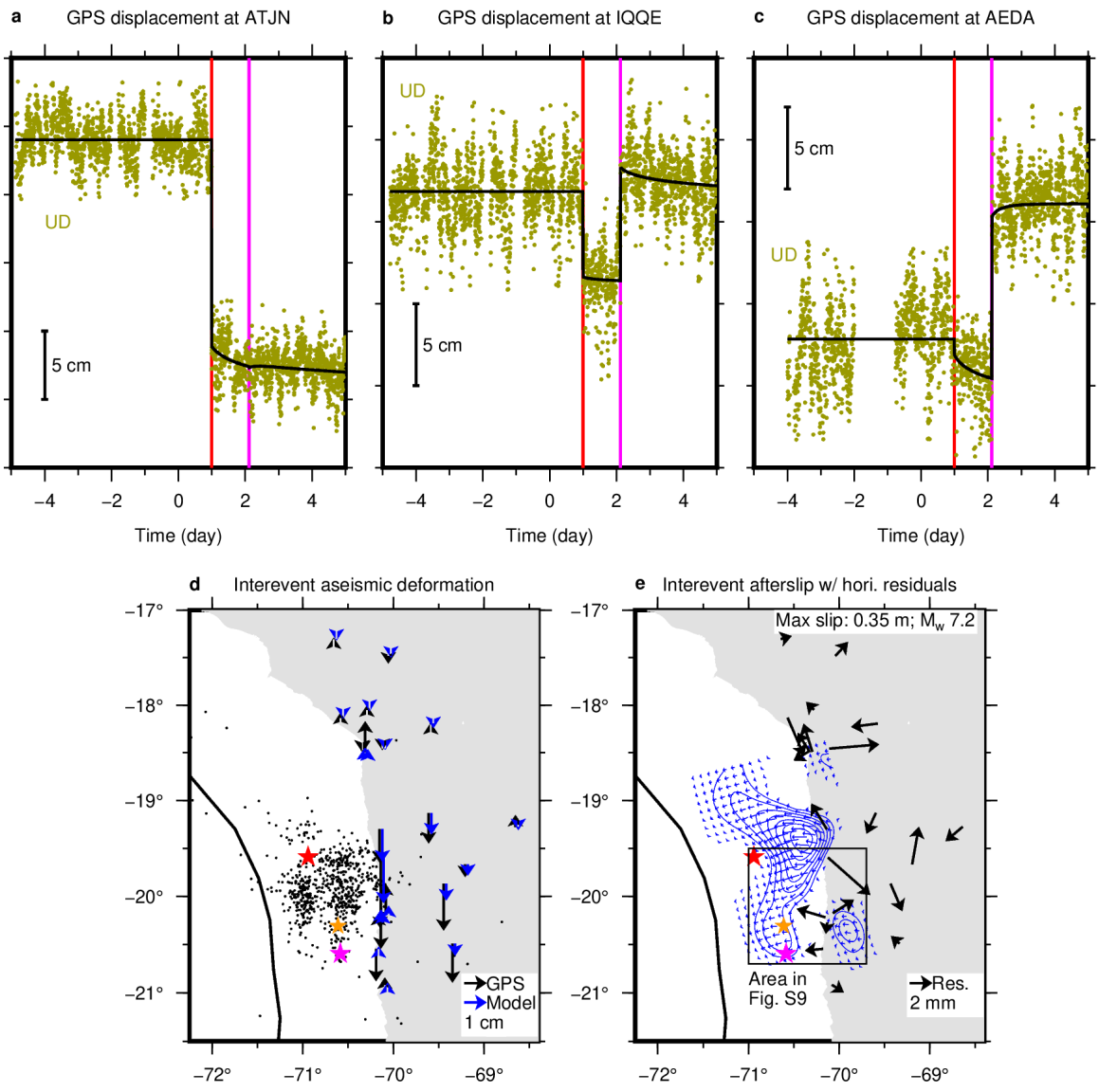

Figure S2. Data analysis and slip inversion result using the trajectory function fit approach. (a) – (c), Trajectory model fit results for vertical components at three sites as labeled. Location of these sites is shown in Figure 1b. (d) Vertical GPS displacements (black vectors) during 27 hours between the mainshock and the largest aftershock, together with model prediction (blue vectors) from aseismic slip inversion shown in (e) and Figure 2a. Refer to Figure 3 for other elements. (e) The inferred interevent afterslip (blue contours) with normalized slip vectors. Black vectors indicate horizontal residuals of the inversion (GPS – Model in Figure 1b).

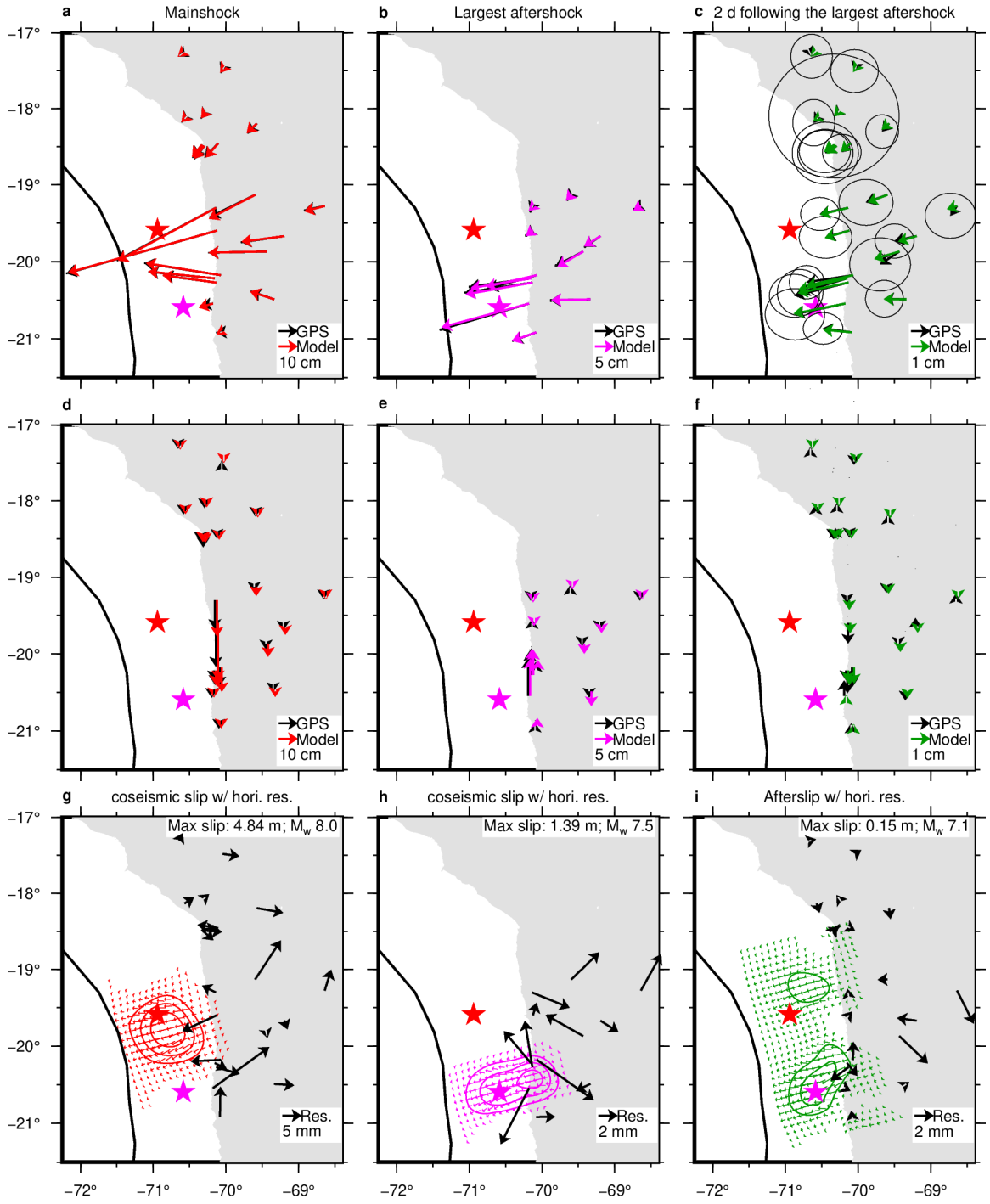

Figure S3. Data analysis and inversion results for the mainshock (a, d, and g), the largest aftershock (b, e, and h), and the post-largest-aftershock stage (2 days; c, f, and i). (a-c), Horizontal GPS displacements at each stage derived from the trajectory model fit. (d-f), Same as (a) – (c) but for vertical displacements. (g-i), Slip inversion results (contours) at each stage with normalized slip vectors. Black vectors indicate horizontal residuals of the inversion (GPS – Model).

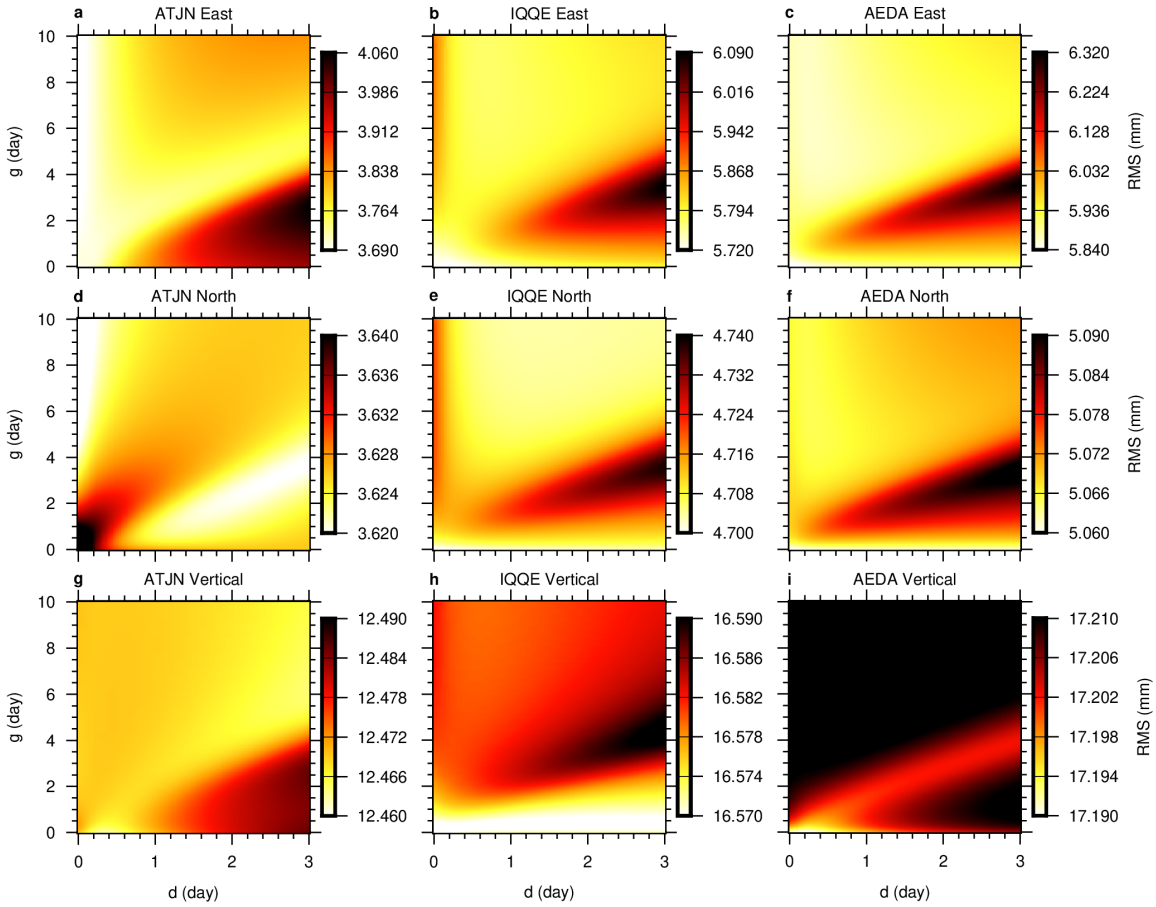

Figure S4. Distribution of RMS of the trajectory model fit with respect to different *d* and *g* in Equation (1) (color). (a-c), Results for the east component at three sites as labeled. Site location is shown in Figure 1b. (d-f) and (g-i) Same as (a) – (c) but for the north and the vertical components, respectively.

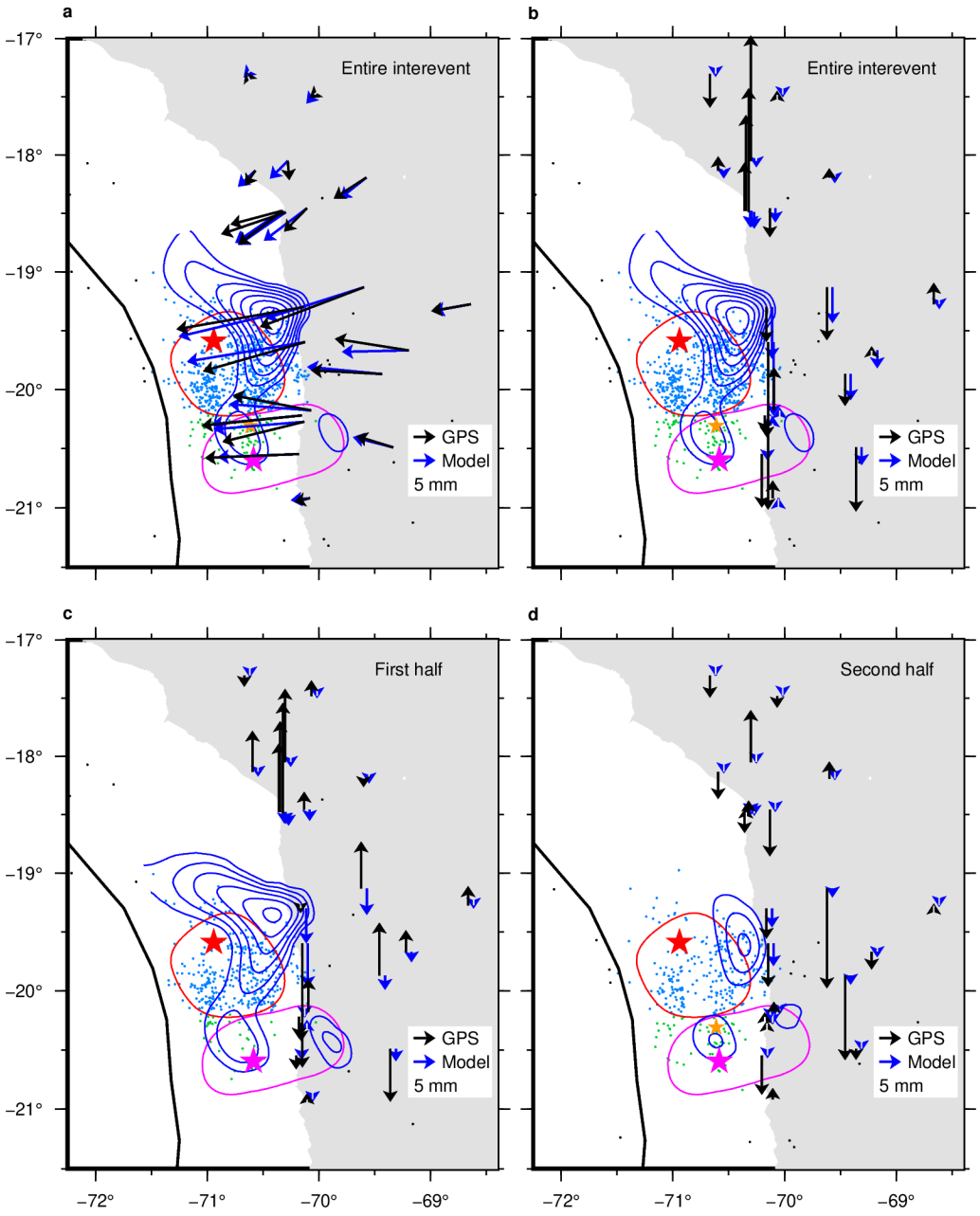

Figure S5. Data analysis and slip inversion result using the moving median approach. (a-b) Cumulative interevent horizontal (a) and vertical (b) displacements (black vectors) derived from the moving median analysis, together with the model prediction (blue vectors) from the inferred afterslip (blue contours). Refer to Figure 2 for other elements. Note that GPS displacements at sites north of 19°S are not inverted. (c-d) Same as Figures 2e-f but with vertical GPS displacements derived from the moving median analysis (black vectors) and model predictions (blue vectors).

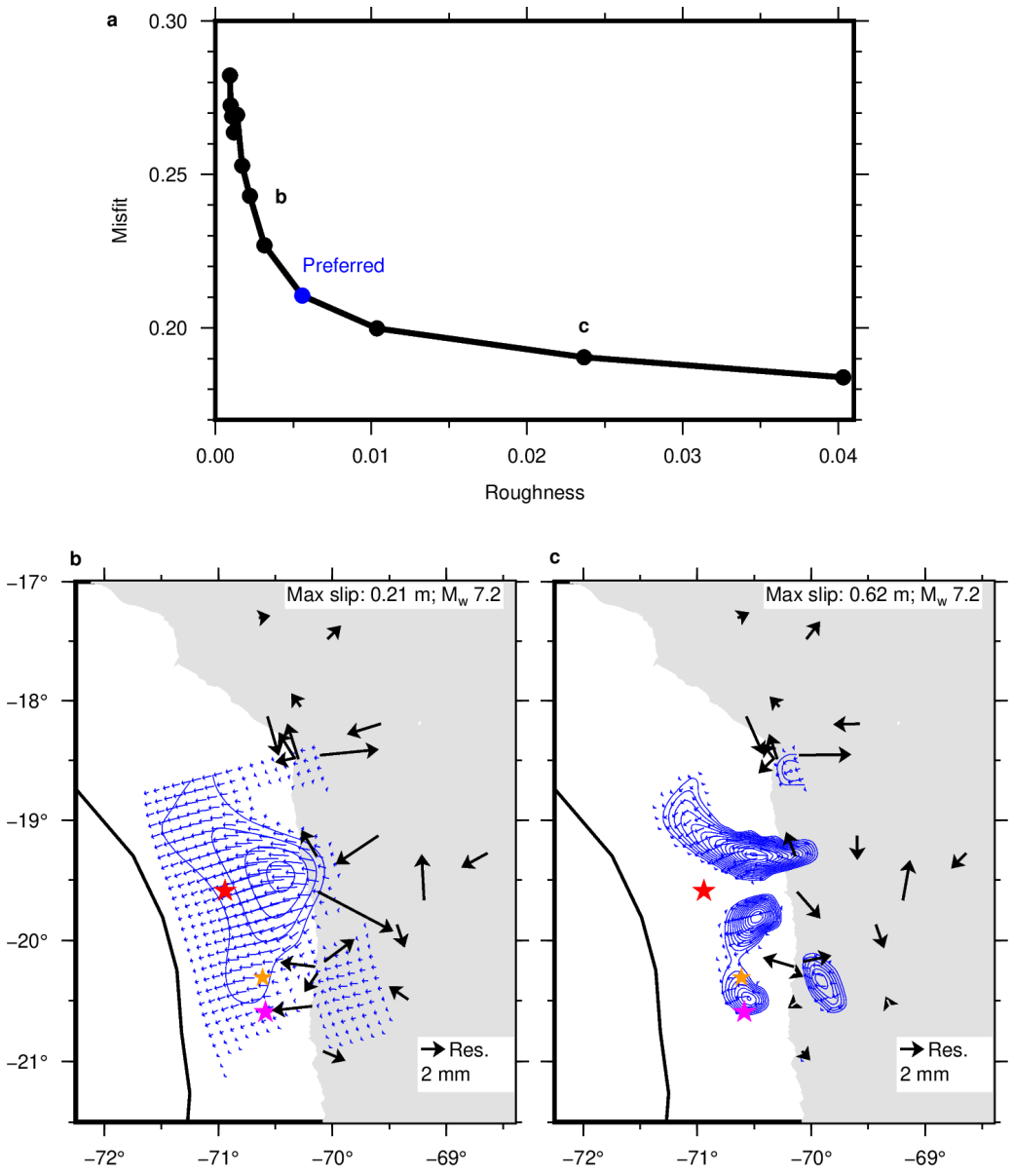

Figure S6. Trade-off curve of the slip roughness and misfit and model variations for the interevent afterslip inversion using the displacements derived from the trajectory model fit. (a) Trade-off curve. Dots indicate preferred (blue) and other tested models. (b-c), model variation with different slip roughness as shown in (a). Refer to Figure S2e for other elements.

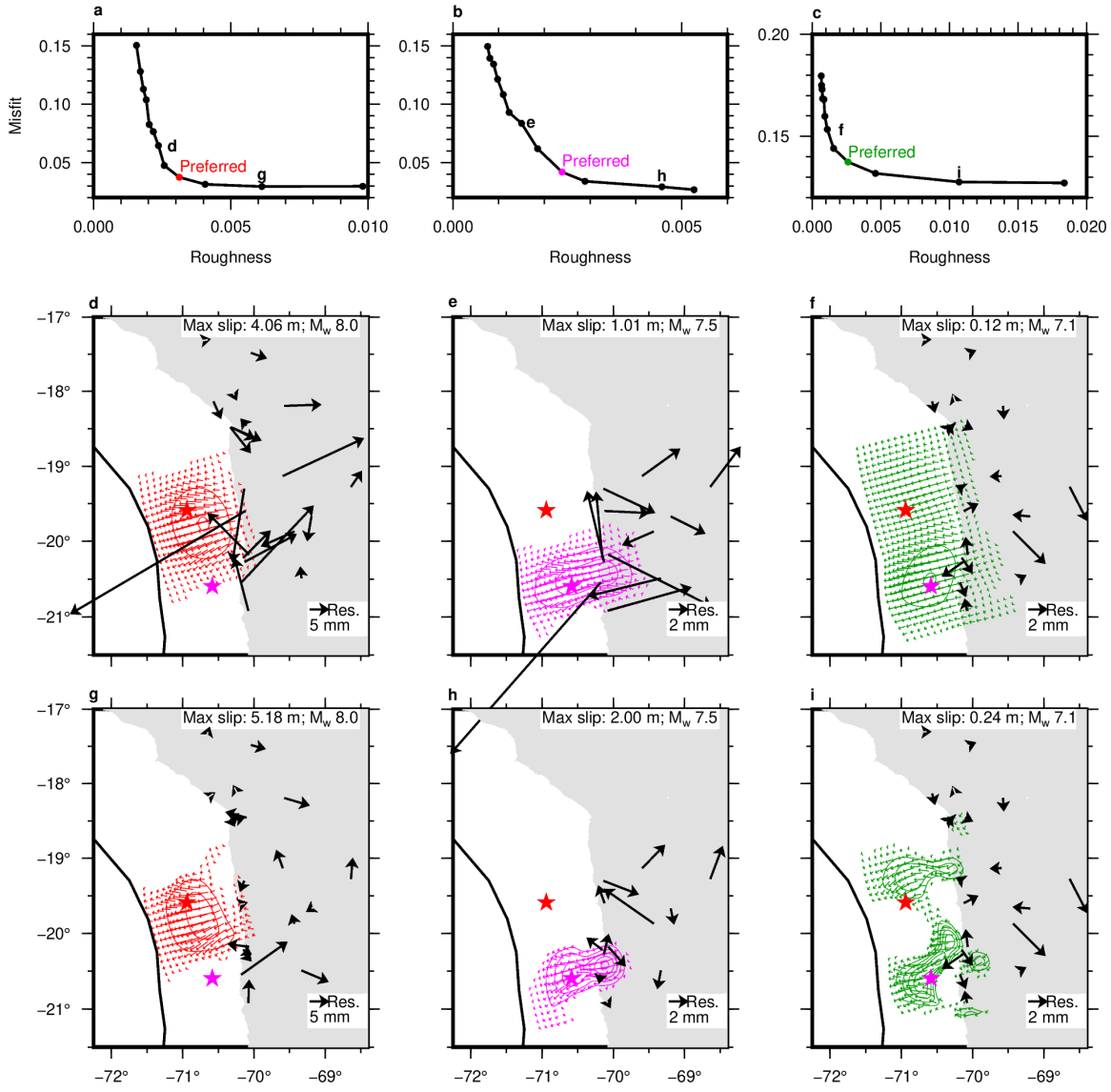

Figure S7. Trade-off curve of the slip roughness and misfit and model variations for the mainshock, the largest aftershock, and subsequent 2-day afterslip. (a-c) Trade-off curve for the mainshock (a), the largest aftershock (b), and subsequent 2-day afterslip (c). Dots indicate preferred (red, purple, or green) and other tested models. (d-i) model variation with different slip roughness as shown in (a) – (c). Refer to Figures S3g-i for other elements.

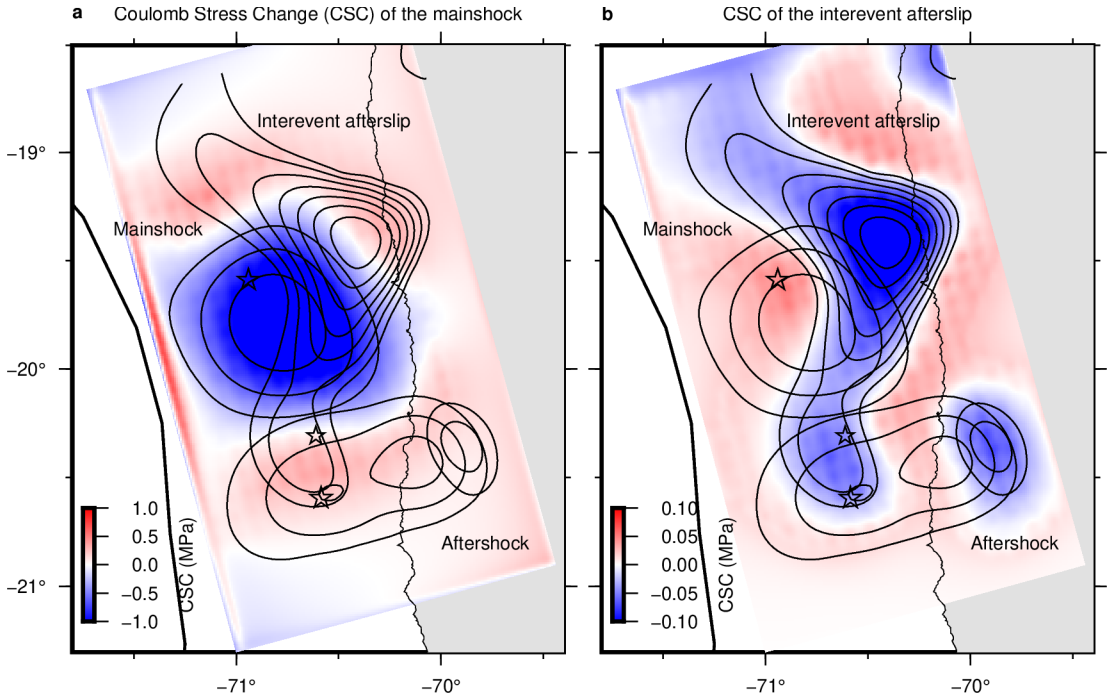

Figure S8. Coulomb stress change (CSC) associated with the mainshock (a) and the interevent afterslip (b). Solid contours are slip distribution of the mainshock, the interevent afterslip, and the largest aftershock, as labeled. Refer to Figure 3 for contour interval and open stars.

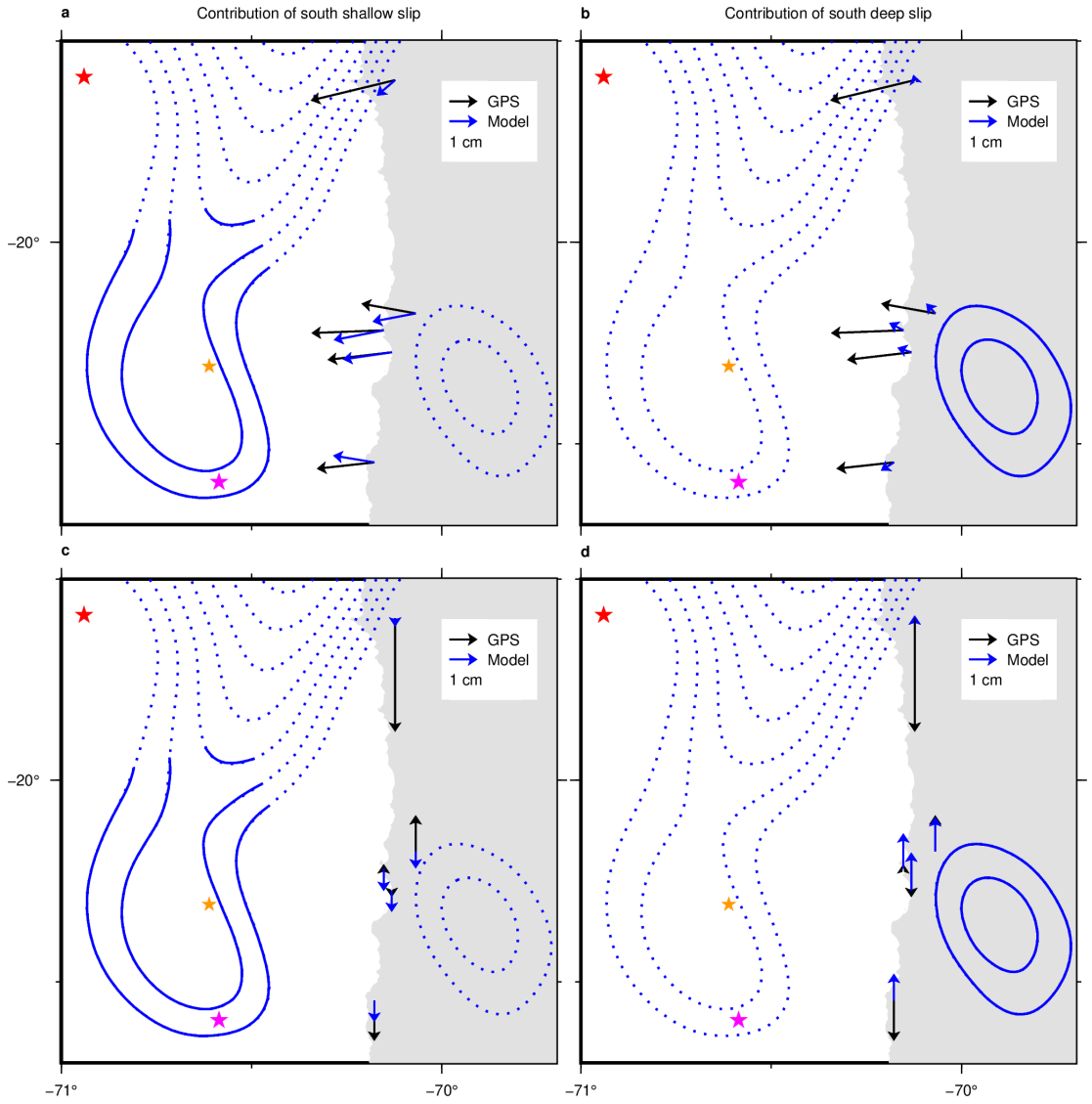

Figure S9. Forward modeling test results for the interevent afterslip. Comparison of interevent GPS displacements derived from the trajectory model fit (black) and model prediction (blue) computed from a subset (solid contours) of interevent afterslip inferred from the black vectors (solid + dot contours). (a-b), Comparison of horizontal displacements. (c-d), Same as (a) – (b) but for vertical displacements. Refer to Figure S2e to identify the plot area.

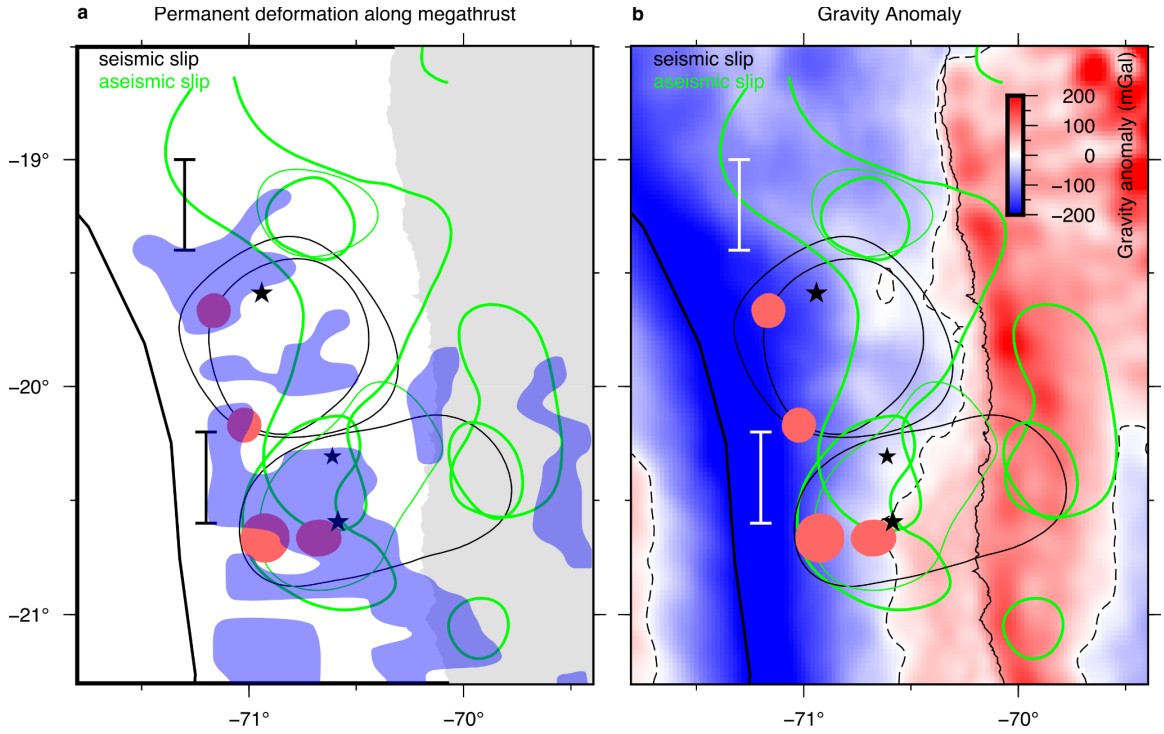

Figure S10. (a) Slip events at different stages with outlines of areas possibly hosting multiple faults subparallel to the megathrust (Cubas et al., 2022) (blue shapes). For clarity, seismic and aseismic slip events at different stages (Figure 4a) are drawn with black and green contours, respectively. (b) Same as A but with gravity anomaly (Sandwell et al., 2014) (background color) with zero value outlined with broken contours. Refer to Figure 1a for other elements.